



HAL
open science

WIKIBrainStem: An online atlas to manually segment the human brainstem at the mesoscopic scale from ultrahigh field MRI

François Lechanoine, Timothée Jacquesson, Justine Beaujoin, Barthélemy Serres, Mohammad Mohammadi, Alexia Planty-Bonjour, Frédéric Andersson, Fabrice Poupon, Cyril Poupon, Christophe Destrieux

► To cite this version:

François Lechanoine, Timothée Jacquesson, Justine Beaujoin, Barthélemy Serres, Mohammad Mohammadi, et al. WIKIBrainStem: An online atlas to manually segment the human brainstem at the mesoscopic scale from ultrahigh field MRI. *NeuroImage*, 2021, 236, pp.118080. 10.1016/j.neuroimage.2021.118080 . hal-03706799

HAL Id: hal-03706799

<https://hal.science/hal-03706799>

Submitted on 9 May 2023

HAL is a multi-disciplinary open access archive for the deposit and dissemination of scientific research documents, whether they are published or not. The documents may come from teaching and research institutions in France or abroad, or from public or private research centers.

L'archive ouverte pluridisciplinaire **HAL**, est destinée au dépôt et à la diffusion de documents scientifiques de niveau recherche, publiés ou non, émanant des établissements d'enseignement et de recherche français ou étrangers, des laboratoires publics ou privés.



Distributed under a Creative Commons Attribution - NonCommercial 4.0 International License

WIKIBrainStem: an online atlas to manually segment the human brainstem at the mesoscopic scale from ultrahigh field MRI.

François Lechanoine^{a, b §}, Timothée Jacquesson^{c §}, Justine Beaujoin^d, Barthélemy Serres^{e, f},
Mohammad Mohammadi^a, Alexia Planty-Bonjour^{a, b}, Frédéric Andersson^a, Fabrice Poupon^d, Cyril
Poupon^{d*}, Christophe Destrieux^{a, b*}

§: These authors equally contributed to this work

*: These senior authors equally contributed to this work

a: UMR 1253, iBrain, Université de Tours, Inserm, Tours, France

b: CHRU de Tours, Tours, France

c: GREATIS Laboratory CNRS UMR5220, Inserm U1206, INSA-Lyon, University of Lyon 1, Lyon, France

d: BAOBAB, Paris-Saclay University, CNRS, CEA

e: ILIAD3, Université de Tours, Tours, France

f: LIFAT, EA6300, Université de Tours, Tours, France

Corresponding author: Christophe Destrieux
UMR1253, iBrain
10, boulevard Tonnellé
37032 Tours, France
christophe.destrieux@univ-tours.fr

Highlights

- WIKIBrainStem is a web-based atlas of the grey matter structures of the human brainstem
- WIKIBrainStem segments the human brainstem in 115 anatomical classes

- WIKIBrainStem proposes anatomical rules for manually segmenting these structures

Abstract

The brainstem is one of the most densely packed areas of the central nervous system in terms of gray, but also white, matter structures and, therefore, is a highly functional hub. It has mainly been studied by the means of histological techniques, which requires several hundreds of slices with a loss of the 3D coherence of the whole specimen. Access to the inner structure of the brainstem is possible using Magnetic Resonance Imaging (MRI), but this method has a limited spatial resolution and contrast *in vivo*. Here, we scanned an *ex vivo* specimen using an ultra-high field (11.7T) preclinical MRI scanner providing data at a mesoscopic scale for anatomical T2-weighted (100 μ m and 185 μ m isotropic) and diffusion-weighted imaging (300 μ m isotropic). We then proposed a hierarchical segmentation of the inner gray matter of the brainstem and defined a set of rules for each segmented anatomical class. These rules were gathered in a freely accessible web-based application, WIKIBrainStem (<https://fibratlas.univ-tours.fr/brainstems/index.html>), for 99 structures, from which 13 were subdivided into 29 substructures.

This segmentation is, to date, the most detailed one developed from *ex vivo* MRI of the brainstem. This should be regarded as a tool that will be complemented by future results of alternative methods, such as Optical Coherence Tomography, Polarized Light Imaging or histology... This is a mandatory step prior to segmenting multiple specimens, which will be used to create a probabilistic automated segmentation method of *ex vivo*, but also *in vivo*, brainstem and may be used for targeting anatomical structures of interest in managing some degenerative or psychiatric disorders.

Keywords

Brainstem, anatomy, exvivo MRI, atlas

Introduction

The human brainstem is one of the most densely packed areas of the encephalon, containing numerous nuclei and white matter tracts involved in awareness, motor, somesthetic, and vital functions. Its recent choice as a target for deep brain stimulation in several neurological pathologies, such as Parkinson's disease (Okun, 2012) or other movement disorders (Larson, 2014), and psychiatric diseases, such as depression or refractory obsessive compulsive disorder (Ooms et al., 2014), has caused the need to comprehend its anatomy to resurface. However, microstructure and connectivity of the brainstem have mostly been studied on 2D histological stained sections (Afshar et al., 1978; Nieuwenhuys et al., 2008; Nolte, 2008; Paxinos and Huang, 1995), a method that loses the 3D coherence of anatomical specimens and renders multiplanar reconstruction quite difficult. Due to these limitations and to the delicate processing of hundreds of serial histological slices, no probabilistic atlas of the whole brainstem is currently available. Magnetic Resonance Imaging (MRI) is an appealing approach to, in a non-destructive manner, obtain 3D images of the inner structures of the brainstem. Clinical MRI scanners, using 1.5 and 3T magnetic fields, nevertheless provide images in which the internal structure of the brainstem appears relatively homogenous. Additional contrasts can be provided by more advanced sequences, for instance diffusion-weighted imaging that uses strong gradient pulses along various directions of the space that tag the spins of water molecules with phases depending on their positions, thus allowing to sensitize the NMR signal to the endogenous diffusion process. Because it is related to movements occurring at the microscopic scale, which are strongly modulated by the presence of cell membranes acting as obstacles, the obtained diffusion-sensitized signal embeds information regarding the local cellular environment that can be decoded to characterize the local tissue microstructure. Information provided by these methods helps to better delineate anatomical structures (Nagae-Poetscher et al., 2004; Salamon et al.,

2005; Stieltjes et al., 2001; Virta et al., 1999), but the spatial resolution of MRI clinical scanners remains relatively low - in the order of 1mm for 3D anatomical sequences and several millimeters for diffusion-weighted images. The emergence of ultra-high-field clinical MRI systems at 7T allows to extend beyond the millimeter scale *in vivo* both for the anatomical (Dumoulin et al., 2018) and diffusion MRI (Heidemann et al., 2010), but at the expense of longer scan durations. More recently, a novel simultaneous multi-slab, diffusion-weighted sequence was proposed to perform diffusion MRI *in vivo* at the submillimeter resolution at 3T (Setsompop et al., 2018). However, a trade-off must be made to choose between the target diffusion sensitization magnitude and the target spatial resolution. In addition, the specific localization of the brainstem next to the petrous bones, with an important air-tissue interface causing major susceptibility artifacts, and its predisposition to movement induced by the pulsation of blood in posterior fossa arteries are all reasons that make the acquisition of very high-resolution MRI data of the brainstem extremely difficult *in vivo*. This limitation can partially be circumvented using preclinical magnets carrying an extreme magnetic field (11.7T), which allows a higher spatial resolution at the cost of a coil size not compatible with a whole human head. This size (about 60mm in diameter) is, nevertheless, adapted to *ex vivo* brainstem specimens. In addition, *ex vivo* specimens permit very long scanning times that are not biased by physiological noise (respiratory movements or blood pulsation) or motion (Augustinack et al., 2010; McNab et al., 2009; Miller et al., 2011). Conversely, death and specimen fixation induce dramatic changes in T2 relaxation time and diffusion coefficients (D'Arceuil and de Crespigny, 2007; D'Arceuil et al., 2007; Leprince et al., 2015), such as *post-mortem* tissues depicting diffusion coefficients two to five times lower than *in vivo* conditions (D'Arceuil et al., 2007). This must be instrumentally compensated by more powerful gradients - also available in preclinical scanners - to obtain access to high diffusion sensitizations (up to 10,000s/mm²) while keeping the echo time very short (typically smaller than 20ms).

Only a few papers have been published on ultra-high field MRI brainstem anatomy (Calabrese et al., 2015a; Fritz et al., 2019; Rushmore et al., 2020), usually on single subjects, with a limited number of more or less precisely described anatomical classes. This renders difficult the replication of the results on other specimens. One of the explanations, apart from the high cost of such scans, is the lack of a precise anatomical reference usable for *ex vivo* MRI.

The goal of this paper is to propose a set of rules to manually segment ultra-high/extreme field (11.7T) *ex vivo* MR images of the human brainstem in approximately 120 hierarchically organized anatomical classes. These rules were assembled in a publicly available web-based application, WIKIBrainStem (<https://fibratlas.univ-tours.fr/brainstems/index.html>), providing a 3D representation and a set of rules for reproducibly segmenting the brainstem. Such a tool is a mandatory step towards an automated atlas of the human brainstem.

Materials and Methods

Specimen preparation and acquisition

One brainstem was obtained from body donation from a subject without a history of neurological or vascular diseases. The brain was extracted less than 24 hours after death and fixed in a 10% formalin solution in distilled water for 3 months. The brainstem was then split from the cerebellum and diencephalon to obtain a specimen compatible with the coil size (60mm in diameter). To partially compensate for effects of formalin fixation by increasing the T2, T2* and diffusion coefficient, the specimen was soaked for 3 weeks in a 0.1M phosphate-buffered saline solution (PBS) at 4°C prior to scanning (Leprince et al., 2015). A specific cylindrical container was manufactured to exactly fit the inner diameter (60 mm) of the MR coil and to avoid air bubbles responsible for imaging artifacts. To stabilize its temperature at 20°C, the specimen was positioned within this container and transferred to the magnet room 4 to 5 hours prior to

scanning. This was required to limit effects related to temperature variations that possibly induce modifications in the local T2 and the local apparent diffusion coefficient (ADC) (Thelwall et al., 2006). To avoid specimen desiccation during acquisition and to reduce imaging artifacts, the sample was immersed in a proton-free fluid (Fluorinert, FC-40, 3M Company, USA). This fluid does not provide any signal during image acquisitions and has a susceptibility coefficient similar to that of brain tissue, thus reducing susceptibility-related imaging artifacts.

The specimen was then scanned using a preclinical 11.7T Bruker MRI system (BioSpec 117/16 USR Bruker MRI, Etlingen, Germany) equipped with a strong gradient system (maximum gradient magnitude = 780mT/m, slew-rate = 9660T/m/s), as well as a 60mm transmit/receive volume coil. The choice of a volume-versus-surface coil was motivated by the need for a homogeneous excitation profile over the large field of view of the brainstem despite a reduced signal-to-noise ratio with volume coils. The B1 field homogeneity also comes with a constant noise model over the field of view, which is also recommended for the noise removal of diffusion-weighted MRI data. The imaging protocol included anatomical and diffusion scans. Anatomical images were acquired using a 3D T2-weighted spin-echo sequence with isotropic spatial resolution of 100 μm and 185 μm , matrix 500x512; 800 slices, TR/TE=500/20 ms, and a total scan time of 35h33min. A single-shell *High Angular Resolution Diffusion Imaging* (HARDI) dataset was acquired using a conventional 2D Pulsed-Gradient Spin-Echo (PGSE) sequence. The *b*-value, characterizing the gradients used to measure diffusion, was chosen to 4500 s/mm^2 to compensate for *post-mortem* loss of contrast. Diffusion data were acquired along 400 directions uniformly distributed over a sphere and split into 12 blocks of 31 directions and one of 28 due to memory limitation of the MRI system and to limit heating of the specimen, which is prone to induce artifacts. For each block, two *b*=0 images (without diffusion ponderation) were acquired. Scanning parameters were as follows: isotropic spatial resolution of 300 μm ; TR/TE= 9000/24.6ms; Δ/δ = 14.4/4.3ms; matrix size: 167x163; 250 slices; and a total scan time of 5 days

7

and 18 hours. The diffusion tensor was calculated for each voxel using a weighted least-squares approach to generate various tensor derived scalar maps including fractional anisotropy (FA), mean diffusivity (MD), and color-encoded direction (CED - RGB code) maps. Microstructural and connectivity data obtained from the HARDI acquisition were not used in the frame of the current study focused on anatomical structures, but they will be investigated in another study.

Preprocessing of anatomical and diffusion MRI dataset was done using the freely available Ginkgo ToolBox (Poupon, n.d.) providing a set of processing tools to correct for imaging artifacts and a set of tools to specifically process diffusion MRI data. Anatomical and diffusion MRI datasets were processed at their original resolutions (100 μm and 185 μm for the anatomy and 300 μm for diffusion respectively). First, the 185 μm resolution anatomical MRI dataset and the 300 μm diffusion MRI dataset at $b=0\text{s}/\text{mm}^2$ were matched to the highest resolution anatomical dataset (at 100 μm), using the 3D affine registration Ginkgo tool relying on the optimization of a mutual information criterion optimized using coarse-to-fine strategy and involving a Nelder-Mead simplex algorithm (Wells et al., 1996). No intensity correction was applied to the anatomical scan to avoid any modification of the raw dataset intensity to be manually segmented. The 12 Diffusion MRI datasets were corrected for noise using the Non Local Means filter of the Ginkgo toolbox assuming a Rician noise model (related to the single-channel transmit-receive coil used to perform the acquisitions) (Wiest-Daesslé et al., 2008). The diffusion MRI acquisitions were performed using a multi-shot PGSE sequence and a high number of shots (33 shots), which allowed to reduce the geometrical distortions related to susceptibility effects or eddy currents to a level which does not require the application of any dedicated correction and, thus, preventing the use of any resampling of the data. Lastly, rotationally invariant DTI maps including the apparent diffusion coefficient (ADC), the fractional anisotropy (FA), the transverse (D_{parallel}) and longitudinal ($D_{\text{perpendicular}}$) diffusion coefficients were computed with a further color-encoded direction map (CED) using a robust fit to ensure the positiveness of the

solution (Fillard et al., 2007). The superimposition of the CED map to the high-resolution anatomical scans contributed to enhance the delineation of brainstem structures while keeping each modality to its native imaging resolution.

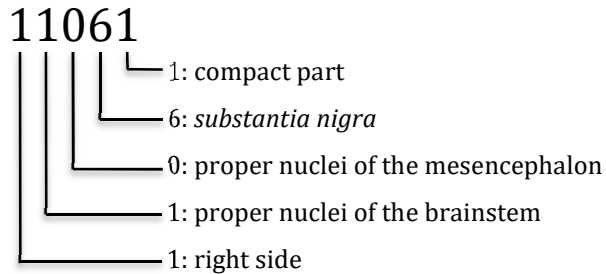
Definition of anatomical classes

We created a highly detailed hierarchical parcellation scheme of the brainstem from a literature review including macroscopic and histologic textbooks (Brodal, 2010; Kamina, 2008; Naidich and Duvernoy, 2009; Nieuwenhuys et al., 2008; Paxinos and Huang, 1995). Brainstem nuclei and sub-nuclei found in the literature were included in a database without knowing *a priori* if they would be visible on the MR data. Some structures not belonging to the brainstem but partially included at the border of the segmented specimen (cerebellar and diencephalic nuclei) were added to this database. A five-digit hierarchical index was assigned to each anatomical class and was stored in the voxels of the segmented volume (Table 1):

- The *first* digit designated the right (1), left (2) or median location of the structure/substructure.
- the *second digit* defined the main group to which the structure belonged: (1) proper nuclei of the brainstem, (2) cranial nerve nuclei, (3-5) reticular nuclei, (6) cerebellar and diencephalic nuclei;
- the *third digit* was related to the location of the structure within these groups; for instance, the proper nuclei of the brainstem were subdivided into mesencephalic (third digit = 0-2), pontine (third digit = 3-5) and medullary nuclei (third digit = 6-9);
- the *fourth digit* designed an anatomical structure;
- finally, a fifth digit equal to "0" was used to consider this structure as a whole; if this structure was subdivided into different anatomical classes, non-null values of the *5th digit* were used; for instance the *substantia nigra* (1/21060) was subdivided into compact

(1/21061) and reticular (1/21062) parts;

For example, the right compact part of the *substantia nigra* was labeled 11061:



Manual segmentation – Definition of segmentation rules

The manual segmentation of the obtained 800 slices was performed using an iMac computer (3,5 GHz Intel Core i7) running High Sierra connected to a combined 27-inch LCD monitor and graphic tablet and stylus (Wacom Cintiq 22HD). We used the Freeview software, part of the Freesurfer package (<https://surfer.nmr.mgh.harvard.edu/>), which simultaneously displayed coronal, axial, and sagittal planes, plus a 3D rendering of the segmented classes; co-registered anatomical (T2 100 μ m and T2 185 μ m) and diffusion (ADC, FA and CED) maps were superimposed with a user-defined transparency (offset) to obtain an optimal delineation for each anatomical class.

Anatomical classes were sequentially segmented, beginning with the biggest and easily delineable ones (for instance, principal nucleus of the inferior olive or red nucleus) before moving to smaller or ill-limited nuclei (reticular nuclei). A dual-pass process included a first rough segmentation on images with a sufficient diffusion-weighted/T2-weighted contrast (diffusion and/or 185 μ m T2), followed by a refinement step using higher-resolution T2-weighted contrast alone (100 μ m). Each anatomical class was attributed a specific RGB color stored in a dedicated look up table (LUT). Part of the structures listed in the original LUT were

not segmented because they were not yet clearly distinguishable on the datasets. The part of cerebellar and diencephalic nuclei located within the anatomical specimen was also segmented. The segmentation and rules definition were initially performed by one author (FL) and reviewed and adapted by two additional ones (TJ, CD). Each ROI of the segmentation was finally regularized using a 3D approach to discard irregularities stemming from the manual segmentation task: a binary volume was created for the background for each anatomical class; then, these binary volumes were smoothed down (mean filtering with gaussian kernel, sigma=0.5 mm), each voxel containing the probability to belong to the corresponding anatomical class. For each voxel, the anatomical class having the highest probability was searched for across-individual files (anatomical classes and background). The resulting smoothed map was used to build the wiki.

WIKIBrainStem interface

WIKIBrainStem (<https://fibratlas.univ-tours.fr/brainstems/index.html>) is a publicly available WebApp specifically developed by ILIAD3 for this project. It is composed of two components: a 3D viewer and a media wiki. The first one (Figure 1) is based on an open source, WebGL-based javascript library (<https://github.com/xtk/X>). This graphical user interface allows for real-time 3D navigation through the segmented results, represented as vtk files (<https://vtk.org/>). The proposed anatomical hierarchy is displayed using a tree-like menu on the right panel of the application. While the user browses this hierarchical menu, the alpha translucency of the selected structures is modulated to highlight them in a 3D view on the middle panel of the application. This 3D view can be zoomed in and out, and the position of the camera can be interactively changed. Finally, the left panel lists the structures highlighted in the 3D view and contains links pointing to the corresponding wikipages, which are displayed as a pop-up when selected.

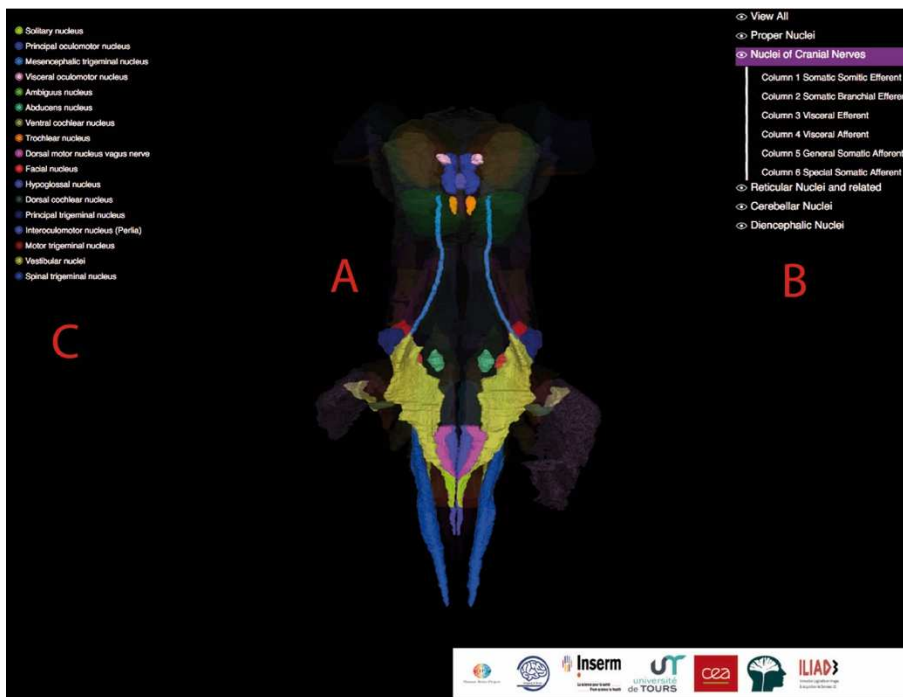


Figure 1: Main page of WIKIBrainStem

A: main window showing an interactive 3D model of the selected structures and brainstem surface. B: hierarchical tree of the main structure groups; C: list of the displayed structures pointing to the corresponding wiki pages.

Original application available at : <https://fibratlas.univ-tours.fr/brainstems/index.html>

The second component of WIKIBrainStem is indeed a media wiki (<https://www.mediawiki.org/wiki/MediaWiki/>) containing a page for each segmented anatomical class, which details as follows (Figure 2):

- basics of its anatomy, function and main connectivity;
- a link to the widely used Uberon ontology (Mungall et al., 2012) entry for this structure.
- the optimal combination of MRI sequences for segmenting this anatomical class (used MR sequence(s) and their related transparency/offset);
- the rules to roughly localize this structure, relatively to surface landmarks or easily recognizable internal structures;
- a precise description of the limits of this structure, related to changes in the various MR contrasts, to surrounding structures or reference planes when no other clear limit was visible;
- and the difficulties we faced during this class segmentation (lack of clear descriptions of its boundaries in the literature, difficulties in visualizing its limits on MR images, choices we were required to make in case of uncertainty...);

- these rules are illustrated by several figures in multiple planes and by an animated 3D model. The current version of WIKIBrainStem contains a total of 52 individual pages, some pages being common to several anatomical classes. Abbreviations used in the text

and figures are the ones proposed by (Paxinos and Huang, 1995)

A

B

C

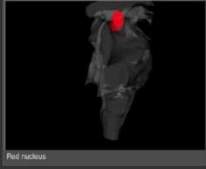
D

E

Red nucleus

Contents Hide

- Group - Substructures
- Anatomy
- Function
- Main connectivity
 - Input
 - Output
- Segmentation rules
 - Color Code
 - Proposed images sets
 - Segmentation method
 - Difficulties
 - References



Red nucleus

Group - Substructures

- Belongs to: proper nuclei of the mesencephalon
- Substructures (not segmented):
 - Parvocellular part or neostrium is the largest one and contains small cells.
 - Magnocellular part or paleostrium contains large cells.
- UBERON: 0001947

Anatomy

- The red nucleus (nucleus ruber, R, 1(R)/2(L)1100) is cranio-caudally ovoid and is about 7mm in diameter.
- It is located within the tegmentum of the mesencephalon, dorso-medial to the substantia nigra.
- Its macroscopic pink-red color is due to its iron content.

Function

Motor control of proximal muscles and tone; coordination between distal muscles of superior limbs and proximal muscles of lower limbs during walking.

Main connectivity

Input

- Cerebellum: the contralateral dentate nucleus projects to the red nucleus through the superior cerebellar peduncle.
- Cerebral cortex, sensorimotor and associative.

Output

- Parvocellular part projects onto the principal nucleus of the inferior olive via the central tegmental tract.
- Magnocellular part projects contralaterally (ventral tegmental decussation):
 - to the spinal cord (subspinal tract), where it is connected to interneurons of lamina VII controlling the motoneurons of lamina IX for proximal muscles.
 - to brainstem, to motoneurons of the facial nerve nucleus, interneurons in the lateral tegmental field, nucleus of the lateral funiculus.

Segmentation rules

Color Code

red nucleus: 255 0 0 / #FF0000

Proposed images sets

- FACED-RGB map overlay (50%) onto T2 weighted 100µm (100%).
- To distinguish the parvocellular and magnocellular parts, overlay (50%/50%) T2 weighted 100µm onto T2 185µm maps.

Segmentation method

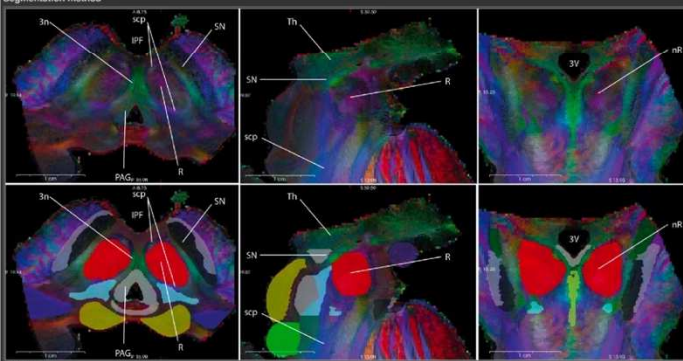


Figure 1

- 1) **Locate the nucleus (Fig.1):**
 - Ovoid, 7mm in diameter.
 - Within the tegmentum of the mesencephalon.
- 2) **Locate the limits of the nucleus (Fig.1):**
 - cranial: thalamus (Th, better seen in green on the sagittal plane) and third ventricle (3V) rostro-medially (see the coronal plane). It is just rostral to the superior colliculus.
 - caudal: enclosed within the superior cerebellar peduncle (scp) containing the dentato-rubro thalamic tract, which is "Y" shaped and blue on sagittal view). On axial view, the nucleus is circled by this tract (blue).
 - ventro-lateral: substantia nigra (SN, black, on axial).
 - ventro-medial: interpeduncular fossa (IPF).
 - dorsal: superior cerebellar peduncle (scp) containing the dentato-rubro thalamic tract and periaqueductal gray (PAG, grey) on axial.
 - medial: ipsilateral intra axial course of the oculomotor nerve (3n, green, axial).
- 3) **Once the limits of the nucleus are defined, begin to draw its outlines on axial, sagittal and coronal views from the middle of the nucleus. Use the obtained "pattern" to achieve its whole segmentation from cranial to caudal on successive axial slices.**

On FA maps, the nucleus is dark, surrounded by several tracts (white).

Difficulties

Quite easy to segment thanks to its spherical shape and because it is surrounded by dense fasciculi.

- Limiting the red nucleus from the following tracts is difficult: central tegmental tract (rubro-olive tract) dorso-caudally, and pretruncal rations (cerebello-rubro-thalamic tract) dorso-medially.
- Distinction between parvocellular and magnocellular parts is difficult (segmented as a whole).

References

- Mai JK, Paxinos G. The Human Nervous System. San Diego: Academic Press; 2012
- Naidich TP, Divernoy HM. Divernoy's atlas of the human brain stem and cerebellum: high-field MRI: surface anatomy, internal structure, vascularization and 3D sectional anatomy. Wien, New York: Springer; 2009
- Nieuwenhuys R, Voogd J, Huijzen Chr van. The human central nervous system. Berlin, New York: Springer; 2008
- Paxinos G, Huang XF. Atlas of the human brainstem. San Diego: Academic Press; 1995

Privacy policy About Brainstem viki Disclaimers


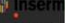







Figure 2: Example of a wiki page for the red nucleus.

Each page gives the following information: A, anatomical details; B, used datasets; C, segmentation rules; D, difficulties; E, 3D model. Original page available at: https://fibratlas.univ-tours.fr/mediawiki/index.php/Red_nucleus

WIKIBrainStem is hosted by Tours University (<http://fibratlas.univ-tours.fr/brainstems/index.html>). Depending on the user internet connection speed, the first download of the 3D objects may require a few seconds to 1 minute. Subsequent downloads are considerably faster thanks to the browser cache.

Data availability

The NIFTI T2-weighted 100 and 185 μ m isotropic anatomic images, the scalar maps derived from diffusion-weighted imaging (FA, CED), and the segmented volume will be freely available under Creative Commons CC BY-NC-SA 4.0 license on the Fibratlas project website (<https://fibratlas.univ-tours.fr/>), along with the LUT table, as well as on the Human Brain Project atlas webpage (<https://ebrains.eu/services/atlas/brain-atlas/>). This format allows the use of the data by any modern imaging software, voxels of the segmented volumes containing the index value of the corresponding anatomical class.

Ethics – Conflicts of interest

The anatomical specimen used in this study was obtained from the Tours body donation program. The donor had previously consented to the terms in which his body would be used for academic or research purposes. The authors do not have any conflict of interest with other parties or organizations that could inappropriately influence their work.

Results

11.7T MRI acquisition and data processing

Anatomical 100 μ m T2 3D Multi Slice Multi Echo series (MSME3D) sequence (Figure 3a and d) provided highly detailed images on which very small nuclei were possibly detected, for instance the trochlear nucleus or the accessory nuclei of the inferior olive. However, the cost of such a

high resolution was a loss of contrast, which sometimes decreased our ability to distinguish two neighboring nuclei. For this reason, we sometimes were required to use anatomical images with a lower resolution (185 μ m) but a higher signal/contrast-to-noise ratio. Major tracts were easily visible on T2 anatomical sequences thanks to their lower signal related to their important myelin content associated with a shorter T2 relaxation time, whereas nuclei appeared in hypersignal, with various shades of gray.

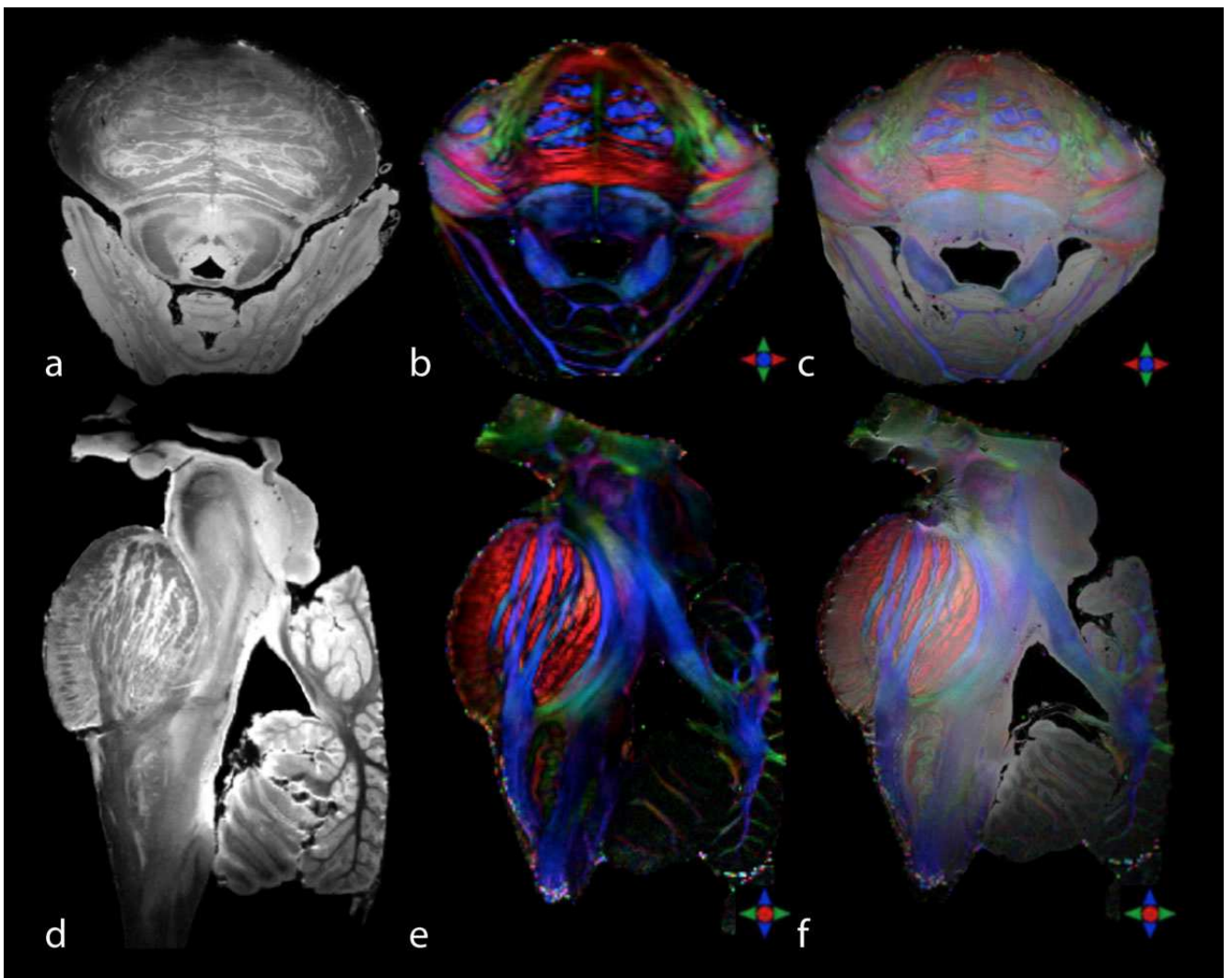


Figure 3. Acquisitions of the brainstem with the Bruker 11.7T preclinical MRI system.

a-c) axial slices; d-f) sagittal slices

a, d) anatomical T2 weighted series; 100 μ m isotropic voxels. Major tracts were easily visible as low signal areas, whereas nuclei appeared lighter, with various shades of gray.

b, e) Diffusion Tensor Imaging (DTI) color-encoded maps; 300 μ m isotropic voxels. Indicators at the bottom right show the color encoding for fibers main direction.

d, f) 50% overlay of color encoded maps onto anatomical T2 series.

Diffusion sequences: ADC, FA and color-encoded direction maps were available at a 300 μ m

isotropic resolution. A favorable contrast between tracts and nuclei was usually present on FA maps, on which the nuclei were black (corresponding to low FA values, possibly due to lower number of fibers or fibers having multiple directions), while the white matter tracts were white (corresponding to high FA values). Nevertheless, the white matter was quite homogeneous on FA maps, making it difficult to precisely delineate the main white matter pathways. FA map was especially useful to segment reticular nuclei, since it showed the intermediate reticular zone (1/23300), which is the main organizer for the classification of the reticular formation proposed by Paxinos (Paxinos and Huang, 1995).

The numerical definition of the optimal contrast windowing for each modality was impossible, because it usually varies at both extremities of the specimen due to a signal drop and may vary across specimens and imaging sessions and parameters. Besides these instrumental limitations, the optimal contrast also depends on the anatomical environment of the segmented anatomical class. For instance, for a given nucleus it should be adapted across slices depending on the density of the surrounding white matter tracts. We, therefore, decided not to provide any numerical value, but to display a large number of figures on WikiBrainStem website to illustrate what we consider a contrast suitable for segmentation.

The overlay rendering of T2-weighted and scalar maps obtained from diffusion was of great assistance in delineating some of the anatomical classes (Figure 3c and f), especially information on orientation and localization of the main white matter pathways derived from CED maps. For example, given their cranio-caudal predominant orientation, the corticospinal tract, medial lemniscus and medial longitudinal fasciculus were displayed blue on CED maps. These fasciculi were not labeled in the atlas but were very valuable landmarks for nuclei segmentation.

Segmentation

Definition of anatomical classes from the literature, description and improvement of the

proposed anatomical rules, redaction of the WIKIBrainStem pages and, finally, segmentation required around 900 hours for the first anatomical expert. Revision of the rules and pages by the two other experts needed approximately 500 additional hours.

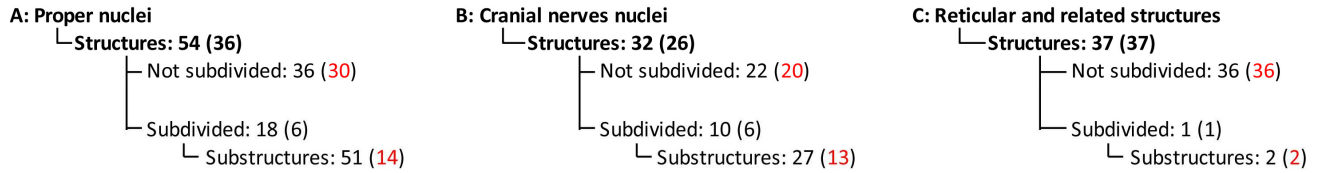


Table 1: number of anatomical structures

The table lists the number of anatomical structures and substructures retained from the literature and currently segmented (in parentheses). Since the subdivided structures may be generated from their divisions, only the substructures and non-subdivided structures (in red) were included in the LUT, for a total 115 anatomical classes: 44 for the proper nuclei of the brainstem (A), 33 for the cranial nerve nuclei (B), and 38 for the reticular formation and related structures (C).

99 brainstem structures defined from the literature were initially retained, from which 29 were subdivided in 80 substructures (Table 1-2). Out of these, it was possible to segment 99 structures and 29 substructures from the MR dataset, and a total of 115 brainstem anatomical classes were included in the LUT (see Table 1 for details). Additionally, 8 structures of the diencephalo-mesencephalic junction and 8 structures of the cerebellum, located at the border of the anatomical specimen, were partially segmented and included in the LUT but not described in the WIKIBrainStem pages. The hierarchical tree of these structures is presented in Table 2 and the volume of each fully segmented anatomical class is given in Table 3 (supplementary material).

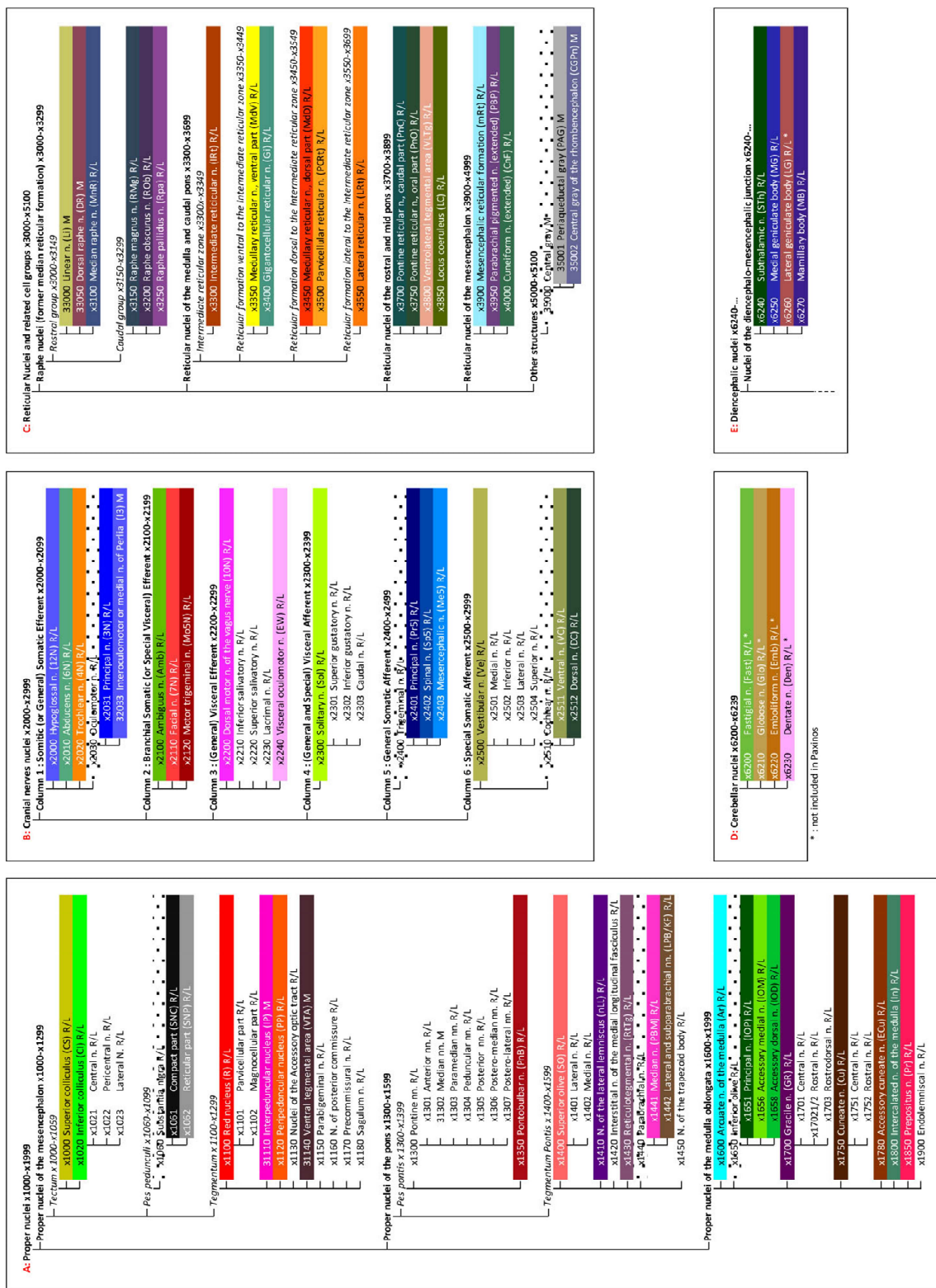


Table 2: Anatomical classes hierarchical list.

All the anatomical classes (structures and substructures) initially retained from the literature are displayed. The ones currently segmented from the dataset are displayed with the color used to display them within the atlas. Structures displayed with a dotted pattern were not directly segmented, but can easily be reconstructed from their segmented substructures. The name of each segmented class is followed by the corresponding abbreviation used in the atlas as defined by Paxinos (Paxinos and Huang, 1995), and by a letter showing if median (M), right (R) or left (L) structure is available.

Groups of anatomical classes are followed by the range of indices of the anatomical classes they contain. The first digit of the index represents the right (1), left (2) or median (3) location of the structure ("x" as first digit of the index is generic for

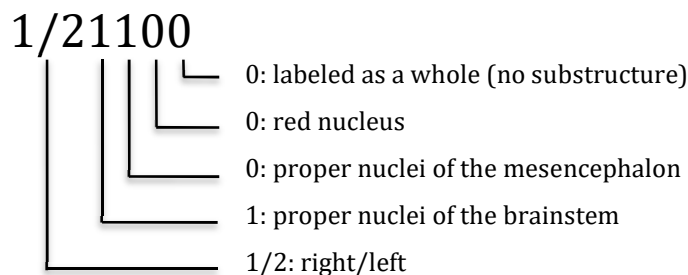
laterality)

Anatomical rules

Anatomical rules are detailed in the wiki for each of the segmented structures/substructures. As an illustration, we present here the segmentation protocol for 4 nuclei to segment with various degrees of difficulty: two easy (red nucleus and principal nucleus of the inferior olive), one difficult (facial n.), and one medium (*Locus Coeruleus*).

Example 1 (easy to segment nucleus): red nucleus

The red nucleus (R), located within the tegmentum of the mesencephalon, was easily segmented because of its elliptical shape and the presence of dense, surrounding tracts providing a strong contrast. Despite initially retained from the literature review, its parvocellular and magnocellular parts were not visible enough to be specifically segmented. It was labeled 1/21100:



It was best observed from FA/CED maps overlaid (50%) onto T2-weighted 100 μ m map (100%). It was first roughly localized within the tegmentum of the mesencephalon, on an axial view running through the rostral third of the superior colliculus. It appeared as an ovoid structure having a diameter of about 7mm. Its limits were defined in every direction as shown in Figure 4.

The limits of round or oval structures, such as R, were then roughly drawn on non-contiguous axial slices to obtain a “pattern”, similar to a loose cage or wicker basket (Figure 5). The latter helps to achieve the segmentation on other planes.

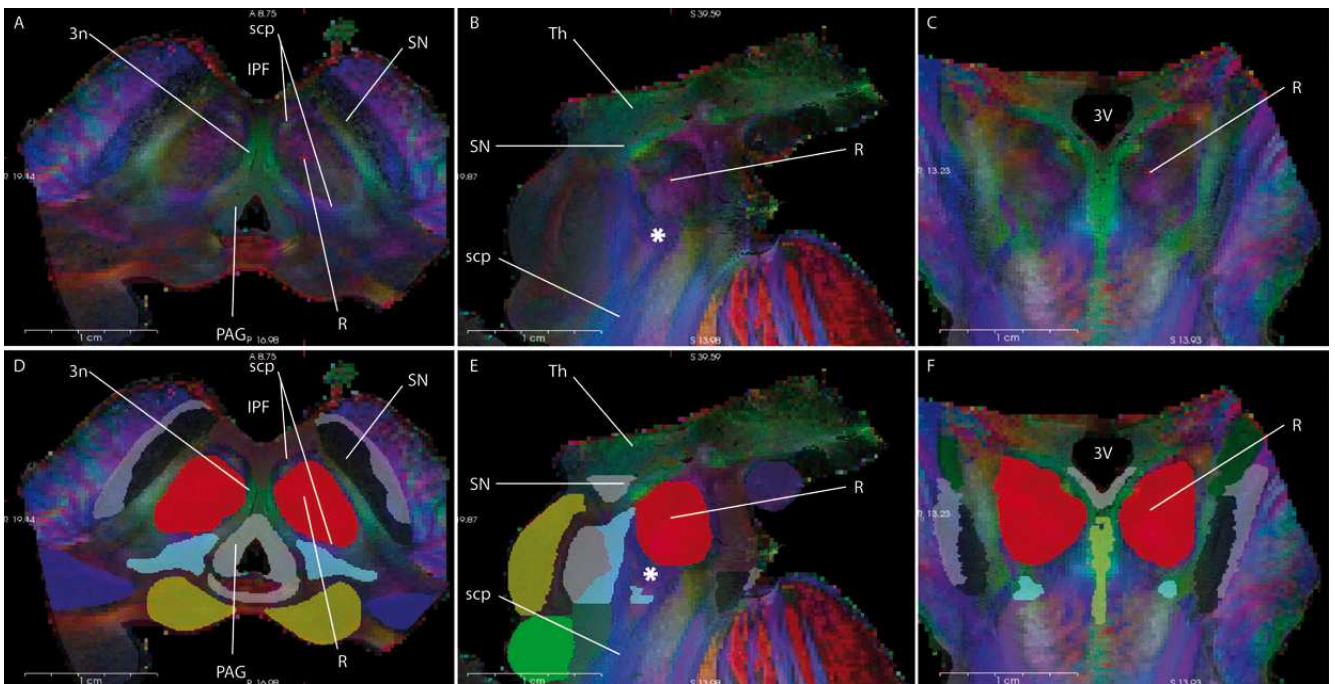


Figure 4: segmentation rules for the red nucleus (R).

R was segmented thanks to the following limits:

- *cranial*: thalamus (Th, better seen in green on the sagittal plane) and third ventricle (3V) rostro-medially.
- *caudal*: enclosed within the superior cerebellar peduncle (scp) containing the dentato-rubro thalamic tract, which is "Y" shaped and blue on sagittal view (*). On axial view, the nucleus is circled by this tract (blue),
- *ventro-lateral*: substantia nigra (SN, black, on axial),
- *ventro-medial*: interpeduncular fossa (IPF),
- *dorsal*: superior cerebellar peduncle (scp) and PAG (grey),
- *medial*: ipsilateral intra axial course of the oculomotor nerve (3n, green, axial).

A, B, C: respectively axial, sagittal and coronal slices, overlay of T2 weighted 100 μm (100% opacity) and CED map (50% transparency). D, E, F: same segmented slices.

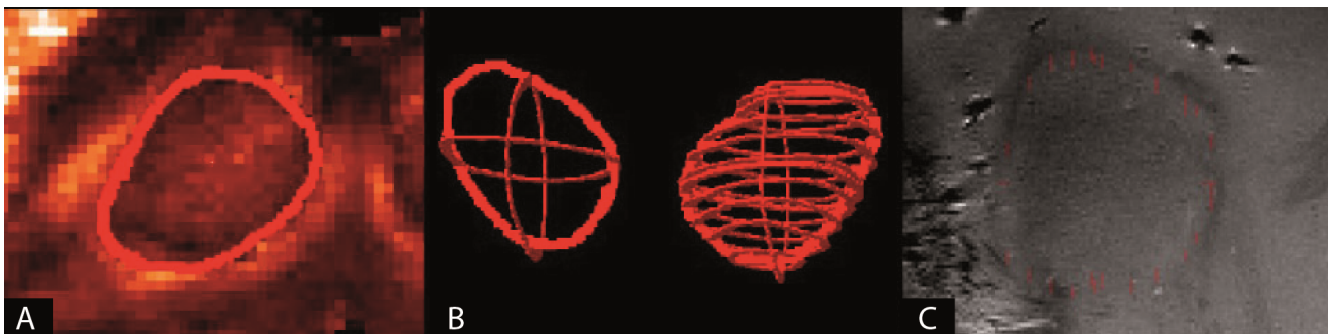


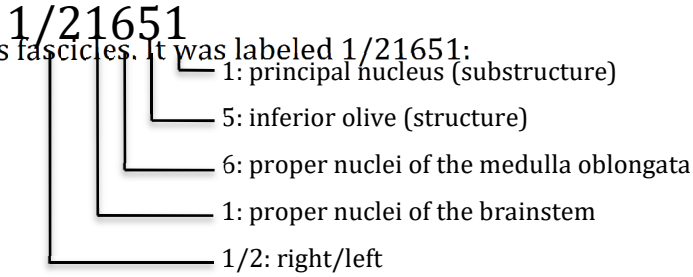
Figure 5: construction of the red nucleus "pattern".

A: non-contiguous slices were segmented mainly from the axial slices. B: resulting "patterns" of both red nuclei, similar to cages or wicker baskets at 2 different steps of segmentation. C: when viewed from another section plane, here coronal, these "patterns" appear as discontinuous dots which help the segmentation of lower contrast areas (for instance caudal pole on this view).

Example 2 (easy to segment nucleus): principal nucleus of the inferior olive

The principal nucleus of the inferior olive (IOPr), located within the ventral *medulla oblongata*,

was also easy to segment due to clear-cut limits on anatomical 100µm images, given many surroundings fascicles. It was labeled 1/21651:



The best combination of MRI used to segment the IOPr was an overlay of CED map (50% transparency) onto T2-weighted MRI at 100µm (100% opacity).

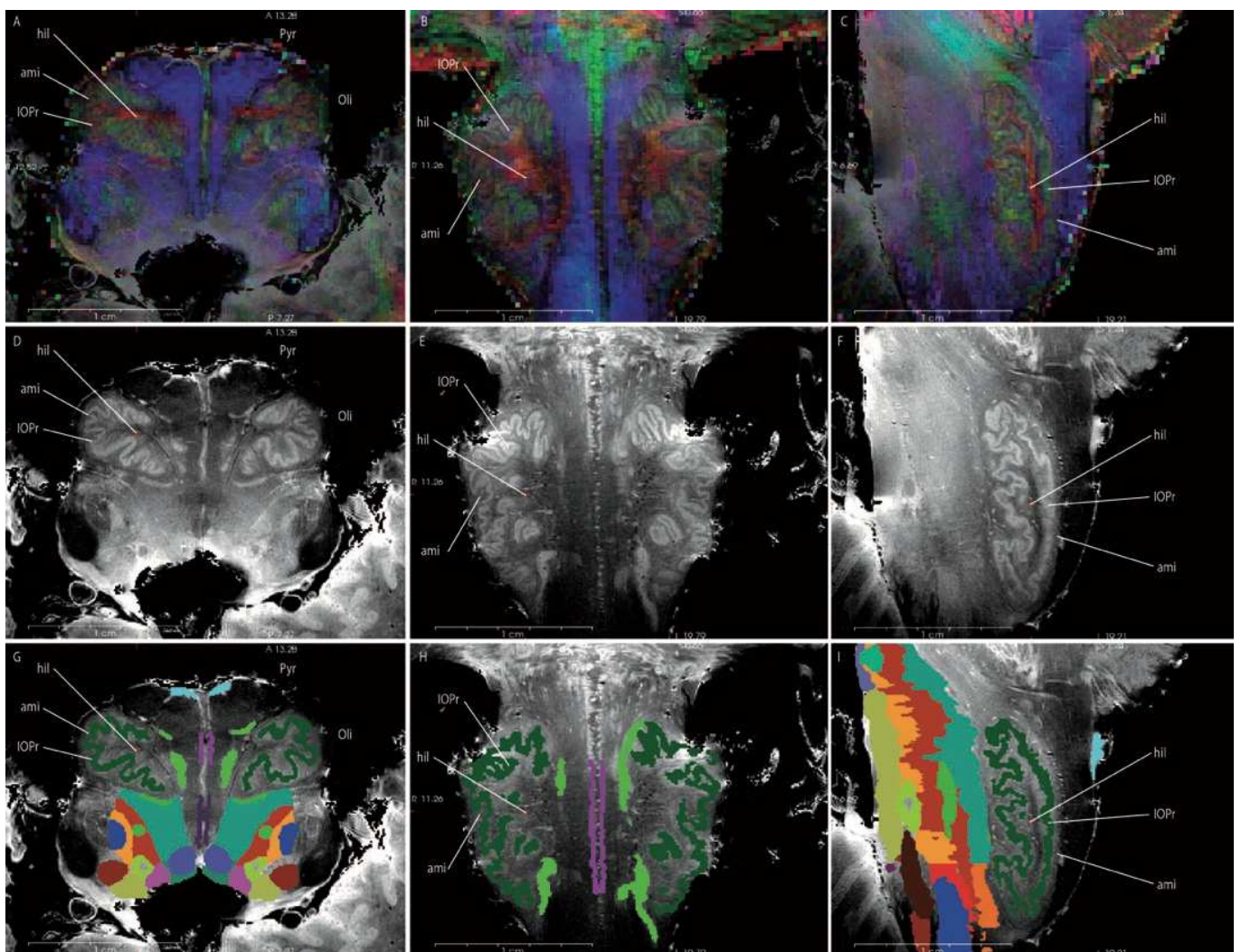


Figure 6: segmentation rules for the principal nucleus of the inferior olive (IOPr)

IOPr was first localized just lateral to the pyramids (Pyr), underneath the olive (Oli). It was easily segmented thanks to its characteristic shape and to the contrast to the surrounding structures:

- externally: the amiculum (ami), forming an external capsule,
- internal: the hilum (hil), easily limited since it contains the spino-olivary tract which appears reddish.

A, B, C: respectively axial, coronal and sagittal slices, overlay of T2 weighted 100 µm (100% opacity) and CED map (50% transparency). D, E, F: same slices on T2 weighted 100 µm. G, H, I: same segmented slices.

It was easy to localize within the ventral part of the rostral medulla oblongata, underneath the surface of the olive, just lateral to the pyramids, thanks to its typical shape evoking a dorso-medially opened purse. The limits of IOPr are detailed in Figure 6, and a 3D rendering provided Figure 7.

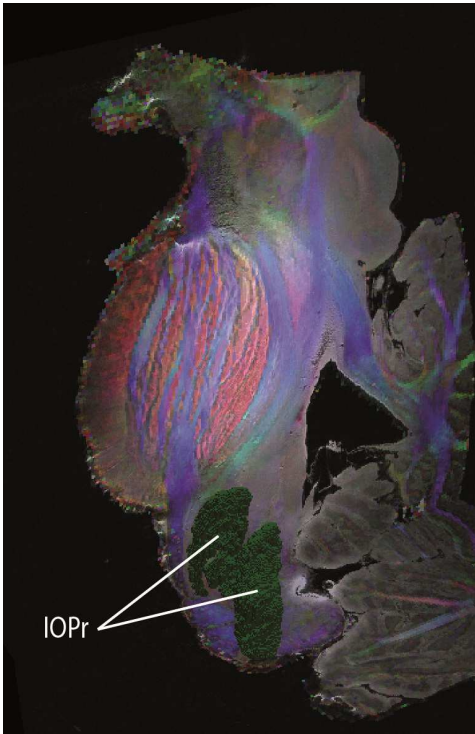
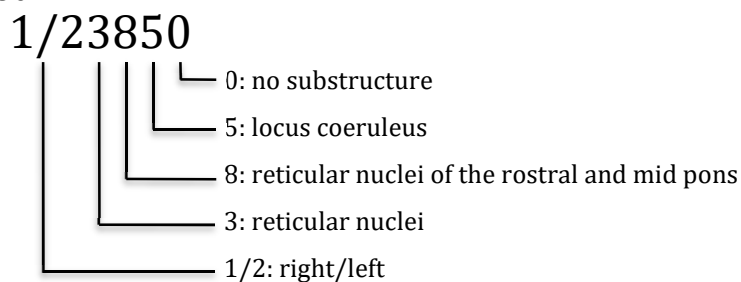


Figure 7: Principal nucleus of the inferior olive (IOPr) overlaid onto sagittal plane.

Example 3 (nucleus of intermediate segmentation difficulty): locus coeruleus

The locus coeruleus (LC) is a major noradrenergic reticular nucleus of the rostral and mid pons, which was labeled 1/23850



It was best seen on T2-weighted MRI dataset at 100µm, on which it appears as a juxtaposition of white and black dots, resulting from an artifact induced by its neuromelanin content (García-Lorenzo et al., 2013). It was almost not visible at a lower resolution. The proposed segmentation rules include a localization step (Figure 8) followed by a definition of the limits, which vary depending on the rostro-caudal level (Figure 9, Figure 10, Figure 11).

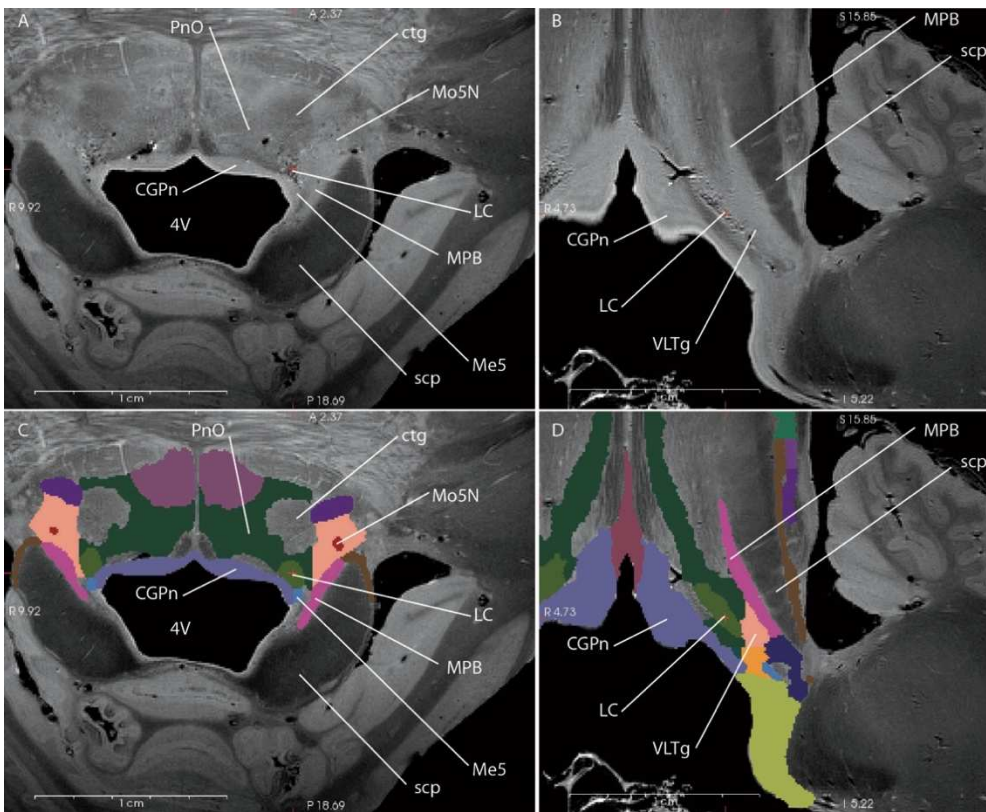


Figure 8: localization of the locus coeruleus (LC)

The reference slice was located at the rostral tip of the motor trigeminal nucleus (Mo5N). The LC was located at the ventro-lateral corner of the 4th ventricle (4V), just ventral to the mesencephalic trigeminal nucleus (Me5), delineated from the 4V by the central gray of the mesencephalon (CGPn). The LC had the aspect of a juxtaposition of white and black dots, resulting from an artifact produced by its neuromelanin content. This artifact was especially clear on T2-weighted 100µm. At lower resolution the LC appeared as a black area which is smaller. It had the shape of an ovoid having its main axis pointing supero-medially.

ctg: centro-tegmental tract; MBP: medial parabrachial n.; PnO: oral part of the pontine reticular formation; scp: superior cerebellar peduncle. A, B: respectively axial and coronal slices, T2 weighted 100 µm. C, D: same segmented slices.

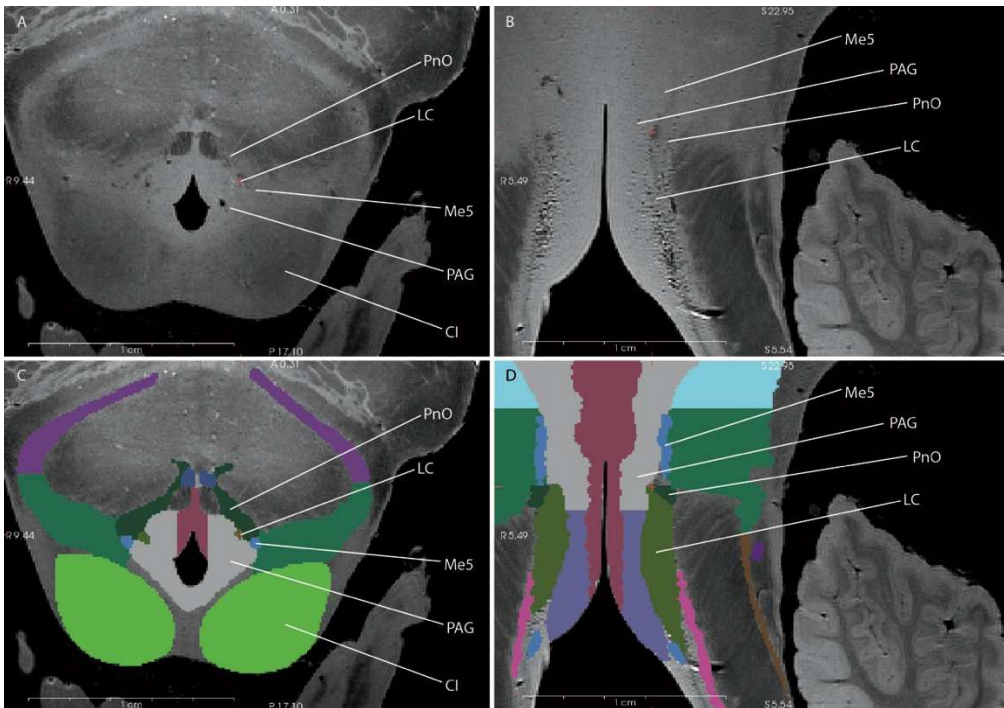


Figure 9: rostral limit of the *Locus coeruleus*

From the reference slice, the artifact was followed on coronal and sagittal views to localize its rostral limit, at the mid rostro-caudal level of the inferior colliculus (CI). At this level, the LC was located:

- between the periaqueductal gray (PAG), ventro-medially, and the oral part of the pontine nucleus (PnO) ventro-laterally;
- it was just ventro-medial to the mesencephalic trigeminal n. (Me5).

A, B: respectively axial and coronal slices, T2 weighted 100 μm . C, D: same segmented slices.

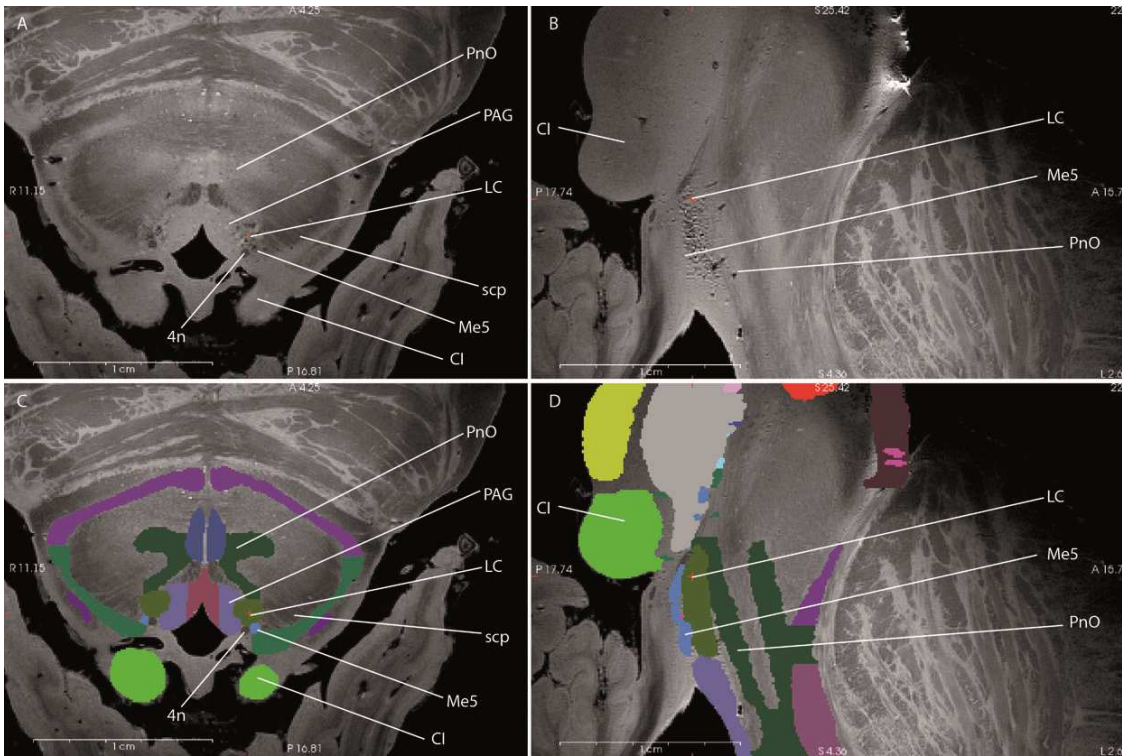


Figure 10: limits of the locus coeruleus (LC) at the caudal pole of the inferior colliculus (CI).

- *ventrally*: oral part of the pontine reticular nucleus (PnO);
- *medially*: central gray of the rhombencephalon (CGPn);
- *dorsally*: mesencephalic trigeminal n. (Me5) laterally, and trochlear nerve (4n) medially;
- *laterally*: superior cerebellar peduncle (scp). More caudally (Figure 8), the medial parabrachial nucleus (MPB) was interposed between the locus LC and scp.

A, B: axial and sagittal slices respectively, T2 weighted 100 μ m. C, D: same segmented slices.

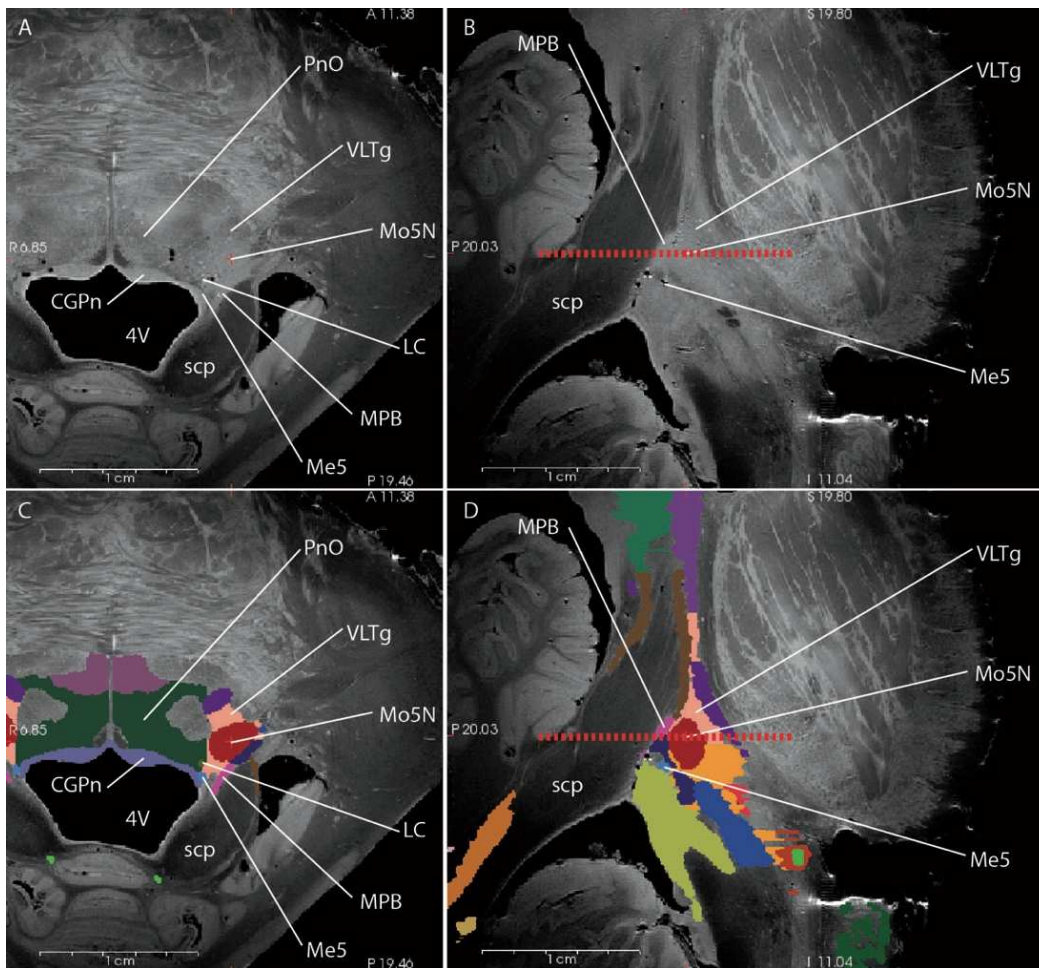


Figure 11: caudal limit of the locus coeruleus (LC)

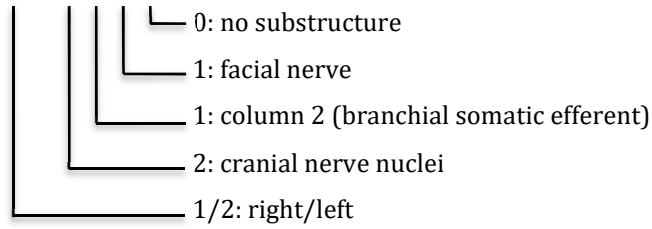
The artifact was followed up to its caudal limit (red dotted line) on coronal and sagittal views. It was located at the level of the rostral 1/4th of the motor trigeminal nucleus (Mo5N).

Me5: mesencephalic trigeminal n.; MBP: medial parabrachial n.; PnO: oral part of the pontine reticular formation; scp: superior cerebellar peduncle; VLTg: ventro-lateral tegmental area; 4V: 4th ventricle. A, B: axial and sagittal slices respectively, T2 weighted 100 μ m. C, D: same segmented slices.

Example 4 (difficult to segment nucleus): Facial nucleus (7N)

7N was more difficult to segment because it was not outlined by surrounding white matter tracts and was in close proximity with the reticular formation of the pons, without any clear contrast. Moreover, facial nerve fibers left the dorsal aspect of the nucleus to curve around the dorsal and then medial aspects of the abducent nucleus, forming the facial colliculus. This isodirectional population of fibers locally increased the FA at the dorsal aspect of the nucleus, making its precise segmentation even more difficult. 7N was identified as 1/22110:

1/22110



The 7N was first localized using CED or T2 weighted 185µm maps (Figure 12). It was then finely segmented using anatomic T2-weighted MRI at 100µm with strong contrast overlaid by CED map (50% transparency).

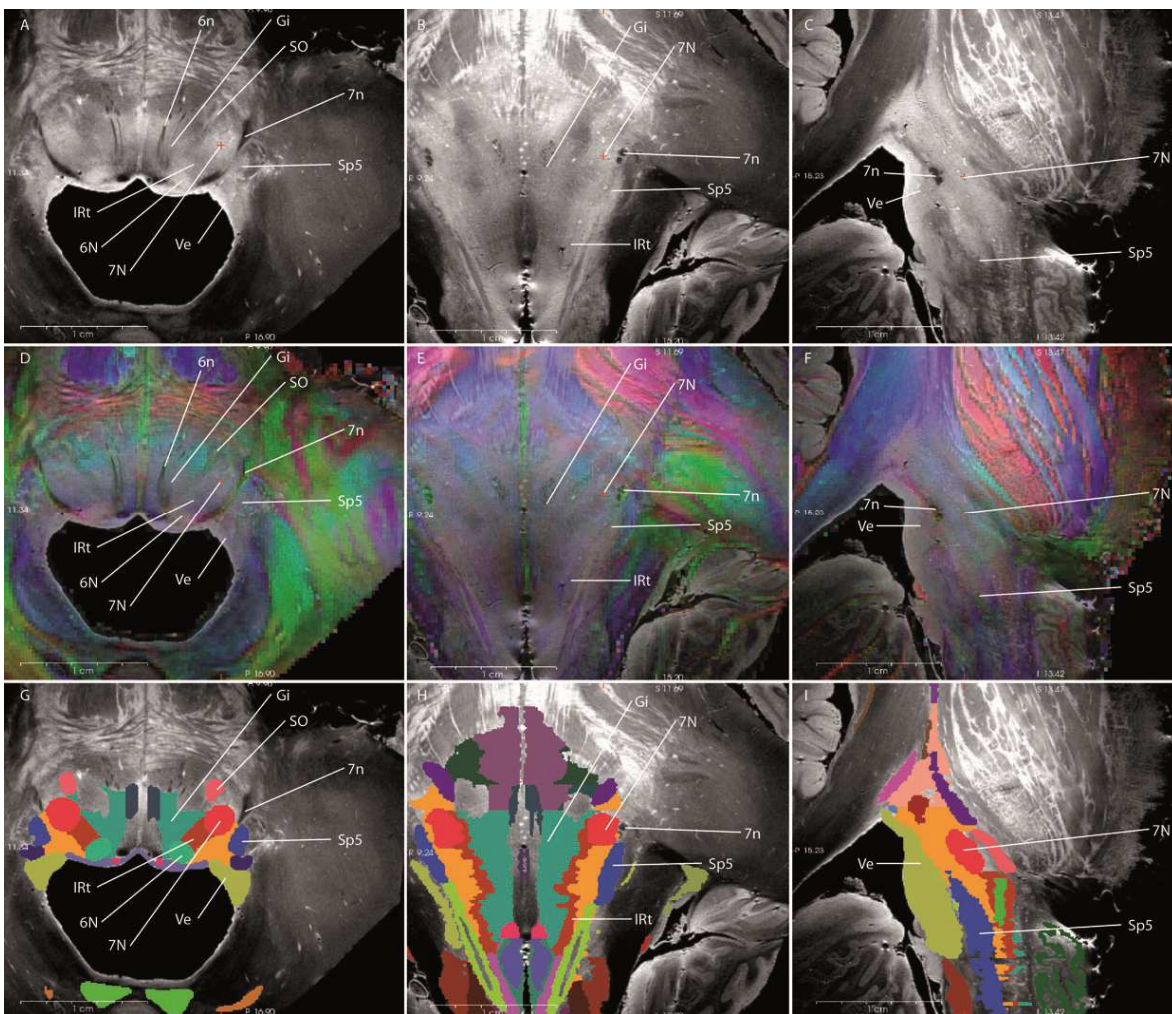


Figure 12: segmentation of the facial nucleus (7N).

CED/T2 185µm maps were used for rough location of 7N: an axial slice running just rostral to the pontomedullary sulcus, through the center of the abducens nucleus (6N) was selected. The facial nerve (7n) appeared as a black linear structure with a ventromedial curve; 7N was round and medial to the 7n. It appeared violet-blue on CED map and was delineated from the 6N by a blue darker area (intermediate reticular zone, IRT).

Then, the limits of 7N were defined:

- cranial and caudal: IRT;

- ventral: superior olivary nucleus (SO);
- dorso-medial: 6N;
- dorsal: vestibular n. (Ve);
- lateral: fibers of 7n and more laterally, spinal trigeminal nucleus (Sp5);
- medial: gigantocellular n. (Gi) in which fibers of the abducent nerve (6n) are running.

A, B, C: respectively axial, coronal and sagittal slices, T2 weighted 100 μm . D, E, F: same slices ; overlay of T2 weighted 100 μm (100% opacity) and CED map (50% transparency). G, H, I: same segmented slices.

Discussion

This paper is the first description of a systematic protocol for brainstem segmentation at the mesoscopic scale from multi-modal MRI contrasts acquired at 11.7T: T2-weighted images at various resolutions, as well as quantitative maps stemming from diffusion-weighted imaging.

Ex vivo MRI is a unique way to non-destructively explore anatomical specimens without losing their 3D coherence. Its use is, nevertheless, questionable since it has its own limitations in terms of spatial resolution and contrast and can be biased by an unknown amount of tissue deformation/artifacts. The choice of optimal imaging data used for segmentation was, indeed, a compromise between spatial resolution and contrast, which is characterized by the signal-to-noise ratio (SNR) and contrast-to-noise ratio (CNR). Among other parameters, the SNR depends on the acquisition time, field strength, and volume of the voxel. For example, doubling the voxel size, from 100 μm to 200 μm isotropic resolution, would multiply the SNR by a factor of 8. This would provide 8 times more signal and, consequently, more contrast to noise ratio. *Ex vivo* imaging benefits from an unlimited scanning time and absence of physiological noise but suffers from a severe drop in T1, T2 and diffusion coefficients that occurs after death and during the fixation process in formalin (D'Arceuil and de Crespigny, 2007; D'Arceuil et al., 2007; Leprince et al., 2015). Immersion in PBS for one week prior to scanning partially reverts this trend (Leprince et al., 2015) but is not efficient enough to obtain usable mesoscopic resolution images in conventional scanners. Using preclinical MRI systems that provide higher values of magnetic field – but also much higher gradient strengths – is, therefore, an appealing solution to study the brainstem anatomy. For instance, the feasibility of a 3D DTI acquisition of the brainstem at 11.7

T has been shown with 125-255 μm isotropic resolution (Aggarwal et al., 2013). This seminal paper was, nevertheless, limited by coil size considerations, because only the medullary-spinal junction was scanned at the highest resolution (125 μm isotropic), whereas the resolution for the whole specimen was 255 μm isotropic. Moreover, the same study used a relatively limited b value and number of directions (4000s/ mm^2 , 30 directions at 255 μm ; 2100 s/ mm^2 , 16 directions at 125 μm), as compared to the one we used (4500/7500/10000 s/ mm^2 , 400 directions), which allows more elaborated modeling of the diffusion process than the simple 6-element tensor model used in (Aggarwal et al., 2013). Despite these limitations, this study was able to show a proper correspondence to myelinstained sections. This was later confirmed at 7T (Calabrese et al., 2015b), with a 50 μm (3D gradient echo pulse sequence) and 200 μm (diffusion data, 4000 s/ mm^2 , 120 directions) isotropic spatial resolution.

To increase the signal-to-noise ratio while preserving the in-plane spatial resolution, most of the brainstem postmortem anatomical and diffusion studies use anisotropic voxels by increasing the slice thickness (Naidich and Duvernoy, 2009; Prats-Galino et al., 2012; Soria et al., 2011). This provides very precise images in the acquisition plane but does not allow for multiplanar nor 3-dimensional reconstructions and, consequently, limits the fine segmentation of internal structures. We deliberately used another approach based on multi-resolution, multi-weighted images; acquisitions were performed at different spatial resolutions and, for some of the segmentation, we used less resolved sections with an enhanced contrast, different weightings (T2, diffusion-derived quantitative maps) or a combination of different images. This method resulted in a combination of adequate spatial resolution and contrast, while preserving 3D reconstructions of the images.

Ex vivo MRI-artifacts were used to recognize some anatomical classes; for instance, the melanin-related hypo-signal was a suitable marker for the *substantia nigra* and *nucleus coeruleus*. Most

artifacts were, nevertheless, undesired, such as small air bubbles responsible for susceptibility artifacts at the surface of the specimen. Other artifacts observed at the fomblin[®]-brainstem interface were especially important at higher resolutions (100 μ m) in areas of small protuberances, such as the caudal part of the inferior colliculus or the upper part of the olive. They led to a certain degree of misregistration of diffusion onto anatomical series at the periphery of the specimen, compelling us to use less resolved T2-weighted images in these areas (185 μ m). However, diffeomorphic registration could be used to improve the alignment of diffusion and anatomical scans in the future.

The proposed anatomical classes have been, of course, previously described in the anatomical or radiological literature (Brodal, 2010; Kamina, 2008; Naidich and Duvernoy, 2009; Nieuwenhuys et al., 2008; Paxinos and Huang, 1995). Nonetheless, to our knowledge, this is the first time that an exhaustive and hierarchical list of anatomical classes has been proposed, associated with step-by-step detailed segmentation protocols.

Every anatomical hierarchical classification is a matter of convention. For instance, Watson (Watson et al., 2019) recently proposed to replace the classical morphological mesencephalon, metencephalon, and myelencephalon classification with a more current form based on genetics, with a more limited extension of the pons. In this work, we chose a classical subdivision of the gray matter of the brainstem, which has anatomical and practical justifications; classes were derived from the Terminologia Anatomica (Federative Committee on Anatomical Terminology, 1998) and major textbooks (Naidich and Duvernoy, 2009; Nieuwenhuys et al., 2008; Paxinos and Huang, 1995), and were logically classified regarding their anatomical location and function. This method also allowed an easy concatenation of nuclei from a given region; Table 2 illustrates the hierarchical tree of the segmented structures and provides the range of index at each level of the classification; for instance, proper nuclei of the mesencephalon located on the right side (first digit 1), left (first digit 2) side, or on the midline (first digit 3), can be pooled by simply

maintaining index classes starting at (1/2/3)¹⁰, (1/2/3)¹¹ or (1/2/3)¹². Additionally to this hierarchical classification, we also described the optimal MRI sequences and the anatomical rules used for this segmentation and rendered this information publicly available through a web application and site. The goal here was to provide a simple protocol, usable on other subjects and by other teams. The original list contained 123 structures, from which 29 were subdivided into 80 substructures. We purposely attempted to be as exhaustive as possible in the list of anatomical classes, to be able to extend our protocol using alternate imaging methods, such as polarized light imaging or optical coherence tomography in the future. Consequently and due to the limited resolution of MRI, only 99 structures were segmented, from which 13 were subdivided in 29 substructures. Despite these limitations, our parcellation is the most complex proposed so far for *ex vivo* MRI of the brainstem. For example, in a recent paper Rushmore (Rushmore et al., 2020) proposed a parcellation of the brainstem specimen previously scanned by Calabrese using a 7T preclinical scanner (Calabrese et al., 2015b). Images were acquired at a spatial resolution of 50 μ m isotropic, but the segmentation was performed after down sampling to 250 μ m. This resulted in the segmentation of the brainstem in only 25 gray matter anatomical classes (50 for both sides).

Some anatomical classes initially retained in the list of potentially segmentable structures were finally not segmented because they were too small to be seen on MRI (often accessory nuclei) due to a lack of contrast with the surrounding structures, or because they were only recognizable at a cellular, neurotransmitter or electrophysiological level. The classification of the reticular nuclei was especially difficult due to their complex and ill-defined anatomy. We, nevertheless, used the classification employed by Paxinos (Paxinos and Huang, 1995), since the intermediate reticular formation was visible from FA maps. Similarly, some structures located at the field of view's border were only partially segmented: dentate nucleus, medial geniculate body, peripeduncular nucleus, subthalamic nucleus, spinal part of the trigeminal nucleus

Conversely, nuclei surrounded by white matter tracts were, indeed, much easier to segment thanks to an enhanced contrast between tracts (hyposignal) and nuclei (hypersignal). An initial delineation of such nuclei was usually performed on the diffusion-weighted quantitative DTI maps (ADC, FA, CED) before being refined on high-resolution anatomical T2-weighted maps (100 μ m). Diffusion sequences alone were, indeed, not sufficient to properly delineate nuclei, because some of them were crossed by, or contained, a large population of fibers; if an isodirectional population of fibers was connected with or arose from a nucleus, the FA increased at the level of the junction, and the fibers/nucleus contrast locally decreased. This was, for instance, the case for the posterior part of the facial nerve. Similarly, since FA reflects the overall directionality inside a voxel, it descended in areas where fibers crossed; if the resulting low-FA area was located close to a nucleus (also having a low FA value), the latter was artificially extended. In these cases, we were obligated to define arbitrary – but tentatively reproducible – rules that, of course, remain debatable. Future experiments will consist of investigating the potential of HARDI models to better disentangle such complex fiber configurations, but this is out of the scope of the current study.

Any segmentation protocol based on anatomical rules indeed contains a certain degree of arbitrariness and aims at providing a consensual and reproducible, if not perfect, parcellation scheme. An ideal validation for a dataset of smaller size would classically include multiple segmentations performed by different users of various levels of expertise and computation of similarity indices. Such a process seemed unrealistic for a 500-hour-long segmentation, since it would test a mixture of rule reliability and procedure tediousness. For this reason, the initial segmentation was performed by a single operator and reviewed by two senior authors who finally provided consensus-based segmentation and rules. A direct comparison of the segmentation performed on MR data to histological or OCT or PLI data on the same specimen would also be of great interest. Nevertheless, this has probably to be more regarded as the

addition of extra data than a direct validation; since these methods use different physical phenomena (optical transmission/attenuation, birefringence, magnetic resonance), a perfect correspondence between the borders of a given anatomical structure studied by different methods seems unlikely at a high resolution, despite a rough match being found at a lower resolution (Solsberg, 1990). Moreover, a comparison to histology would not completely solve the problem, because ambiguities remain even for the segmentation of immuno-histochemical stained slices (Brodal, 2010; Kamina, 2008; Naidich and Duvernoy, 2009; Nieuwenhuys et al., 2008; Paxinos and Huang, 1995). The structure of WIKIBrainStem will allow its future extension to non-MRI data that may arise from additional studies to be very feasible. In the same vein, the segmentation rules described in this study were developed for the field strength and imaging protocols detailed in the Materials and Methods section. Different acquisition methods, more or less sensitive to the underlying microstructure, as well as the impact of different techniques for specimen preparation, may thus lead to different results. For instance, the volume of the red nucleus, still considered as easy to segment, was measured by several authors (Eapen et al., 2011; Keuken et al., 2017, 2014; Zou et al., 2019) and ranged from 107 to 321 mm³, depending on the used magnetic fields and imaging protocols (right and left red nuclei were measured to 142 and 139 mm³ respectively in our study). Assessing the influence of the imaging parameters, field strength, and specimen preparation methods is far beyond the scope of this work, but the proposed anatomical rules may need to be adapted to very different imaging conditions.

The brainstem is usually considered less variable than the more rostral parts of the encephalon, such as the telencephalon. However, no precise data is currently available on this topic. Although the present anatomical rules were defined from a single anatomical specimen, the definition of each anatomical class greatly depends on its anatomical environment, such as the surrounding tracts and nuclei. Consequently, even if the same region is slightly variable in other specimens, the anatomical rules will be usable. One of the next applications of WIKIBrainStem will be the

33

segmentation of several anatomical specimens by different experts. This will produce probability maps of the brainstem inner structures across subjects, which will be the starting point to propose an automated segmentation protocol, as this has already been performed at lower resolution for the brain (Destrieux et al., 2010). Such a probabilistic atlas of the brainstem defined at very high resolution will later be used for an automated parcellation of lower resolution images obtained from clinical MRI systems (1,5 or 3T). This would lead to a probabilistic localization of the nuclei from *in vivo* data at a resolution at which they are obviously not visible. The registration process mapping the atlas to individual *in vivo* datasets will clearly need to take into account possible distortion related to the specimen extraction and formalin-fixation. For instance, formalin fixation of the brainstem induces a shrinkage of 8.3% in the longitudinal direction, whereas no change is observed transversally (Quester and Schroder, 1997).

Conclusion

The protocol of segmentation of the whole brainstem that we developed from high resolution, *ex vivo*, ultra-high field MRI at 11.7 Tesla is the most detailed to date. The proposed segmentation rules were gathered in a web-based application and site, which are freely available to the public. This represents a first step towards the creation of a multi-subject probabilistic atlas of the brainstem, applicable to automatically segment high-resolution, but also clinical images. This would certainly help with the precise localization of brainstem lesions (vascular, traumatic or tumoral), choice of the most appropriate surgical approaches and to precisely delineate anatomical targets for deep brain stimulation.

Acknowledgements

We express our gratitude to the donor involved in the body donation program of the Association

des dons du corps du Centre Ouest, Tours, who made this study possible by generously donating his body to scientific research. We also acknowledge Mr G erald Deluermoz (universit  de Tours) who extracted the anatomical specimen and Rudolf Hergesheimer for editing the manuscript.

Funding: this project/research has received funding from the European Union's Horizon 2020 Framework Program for Research and Innovation under the Specific Grant Agreement No. 945539 (Human Brain Project SGA3). It also benefited from a specimen collected in the frame of the 2014 Agence Nationale de la Recherche 14-CE17-0015-01 project. FL was funded for one year by the Agence R gionale de Sant  Centre-Val-de-Loire.

REFERENCES

- Afshar, F., Watkins, E., et al., 1978. A variability Study, in: *Stereotaxic Atlas of the Human Brainstem and Cerebellar Nuclei*. Raven Press, New York.
- Aggarwal, M., Zhang, J., Pletnikova, O., Crain, B., Troncoso, J., Mori, S., 2013. Feasibility of creating a high-resolution 3D diffusion tensor imaging based atlas of the human brainstem: A case study at 11.7T. *NeuroImage* 74, 117–127. <https://doi.org/10.1016/j.neuroimage.2013.01.061>
- Augustinack, J.C., Helmer, K., Huber, K.E., Kakunoori, S., Z llei, L., Fischl, B., 2010. Direct visualization of the perforant pathway in the human brain with ex vivo diffusion tensor imaging. *Front. Hum. Neurosci.* 4, 42. <https://doi.org/10.3389/fnhum.2010.00042>
- Brodal, P., 2010. *The central nervous system: structure and function*, 4th ed. ed. Oxford University Press, New York.
- Calabrese, E., Hickey, P., Hulette, C., Zhang, J., Parente, B., Lad, S.P., Johnson, G.A., 2015a. Postmortem diffusion MRI of the human brainstem and thalamus for deep brain stimulator electrode localization: Postmortem Diffusion MRI for DBS Electrode Localization. *Hum. Brain Mapp.* 36, 3167–3178. <https://doi.org/10.1002/hbm.22836>
- Calabrese, E., Hickey, P., Hulette, C., Zhang, J., Parente, B., Lad, S.P., Johnson, G.A., 2015b. Postmortem diffusion MRI of the human brainstem and thalamus for deep brain stimulator electrode localization. *Hum. Brain Mapp.* 36, 3167–3178. <https://doi.org/10.1002/hbm.22836>
- D'Arceuil, H., de Crespigny, A., 2007. The effects of brain tissue decomposition on diffusion tensor imaging and tractography. *Neuroimage* 36, 64–8. <https://doi.org/10.1016/j.neuroimage.2007.02.039>
- D'Arceuil, H.E., Westmoreland, S., de Crespigny, A.J., 2007. An approach to high resolution diffusion tensor imaging in fixed primate brain. *Neuroimage* 35, 553–65. <https://doi.org/10.1016/j.neuroimage.2006.12.028>
- Destrieux, C., Fischl, B., Dale, A., Halgren, E., 2010. Automatic parcellation of human cortical gyri and sulci using standard anatomical nomenclature. *Neuroimage* 53, 1–15.

<https://doi.org/10.1016/j.neuroimage.2010.06.010>

Dumoulin, S.O., Fracasso, A., van der Zwaag, W., Siero, J.C.W., Petridou, N., 2018. Ultra-high field MRI: Advancing systems neuroscience towards mesoscopic human brain function. *NeuroImage* 168, 345–357. <https://doi.org/10.1016/j.neuroimage.2017.01.028>

Eapen, M., Zald, D.H., Gatenby, J.C., Ding, Z., Gore, J.C., 2011. Using High-Resolution MR Imaging at 7T to Evaluate the Anatomy of the Midbrain Dopaminergic System. *Am. J. Neuroradiol.* 32, 688–694. <https://doi.org/10.3174/ajnr.A2355>

Federative Committee on Anatomical Terminology, 1998. *Terminologia anatomica : international anatomical terminology*. Thieme, Stuttgart ; New York.

Fillard, P., Pennec, X., Arsigny, V., Ayache, N., 2007. Clinical DT-MRI estimation, smoothing, and fiber tracking with log-Euclidean metrics. *IEEE Trans. Med. Imaging* 26, 1472–1482. <https://doi.org/10.1109/TMI.2007.899173>

Fritz, F.J., Sengupta, S., Harms, R.L., Tse, D.H., Poser, B.A., Roebroek, A., 2019. Ultra-high resolution and multi-shell diffusion MRI of intact ex vivo human brains using kT-dSTEAM at 9.4T. *NeuroImage* 202, 116087. <https://doi.org/10.1016/j.neuroimage.2019.116087>

García-Lorenzo, D., Longo-Dos Santos, C., Ewencyk, C., Leu-Semenescu, S., Gallea, C., Quattrocchi, G., Pita Lobo, P., Poupon, C., Benali, H., Arnulf, I., Vidailhet, M., Lehericy, S., 2013. The coeruleus/subcoeruleus complex in rapid eye movement sleep behaviour disorders in Parkinson's disease. *Brain J. Neurol.* 136, 2120–2129. <https://doi.org/10.1093/brain/awt152>

Heidemann, R.M., Porter, D.A., Anwander, A., Feiweier, T., Heberlein, K., Knösche, T.R., Turner, R., 2010. Diffusion imaging in humans at 7T using readout-segmented EPI and GRAPPA. *Magn. Reson. Med.* 64, 9–14. <https://doi.org/10.1002/mrm.22480>

Kamina, P., 2008. *Anatomie Clinique*. Maloine, Paris.

Keuken, M.C., Bazin, P.-L., Backhouse, K., Beekhuizen, S., Himmer, L., Kandola, A., Lafeber, J.J., Prochazkova, L., Trutti, A., Schäfer, A., Turner, R., Forstmann, B.U., 2017. Effects of aging on T1*, T2* , and QSM MRI values in the subcortex. *Brain Struct. Funct.* 222, 2487–2505. <https://doi.org/10.1007/s00429-016-1352-4>

Keuken, M.C., Bazin, P.-L., Crown, L., Hootsmans, J., Laufer, A., Müller-Axt, C., Sier, R., van der Putten, E.J., Schäfer, A., Turner, R., Forstmann, B.U., 2014. Quantifying inter-individual anatomical variability in the subcortex using 7 T structural MRI. *NeuroImage* 94, 40–46. <https://doi.org/10.1016/j.neuroimage.2014.03.032>

Larson, P.S., 2014. Deep brain stimulation for movement disorders. *Neurother. J. Am. Soc. Exp. Neurother.* 11, 465–474. <https://doi.org/10.1007/s13311-014-0274-1>

Leprince, Y., Schmitt, B., Chaillou, É., Destrieux, C., Barantin, L., Vignaud, A., Rivière, D., Poupon, C., 2015. Optimization of sample preparation for MRI of formaldehyde-fixed brains, in: 23rd Annual Meeting of ISMRM. Presented at the 23rd Annual Meeting of ISMRM, Toronto, Canada, p. 2283.

McNab, J.A., Jbabdi, S., Deoni, S.C.L., Douaud, G., Behrens, T.E.J., Miller, K.L., 2009. High resolution diffusion-weighted imaging in fixed human brain using diffusion-weighted steady state free precession. *NeuroImage* 46, 775–785. <https://doi.org/10.1016/j.neuroimage.2009.01.008>

Miller, K.L., Stagg, C.J., Douaud, G., Jbabdi, S., Smith, S.M., Behrens, T.E.J., Jenkinson, M., Chance, S.A., Esiri, M.M., Voets, N.L., Jenkinson, N., Aziz, T.Z., Turner, M.R., Johansen-Berg, H., McNab, J.A., 2011. Diffusion imaging of whole, post-mortem human brains on a clinical MRI scanner. *NeuroImage* 57, 167–181. <https://doi.org/10.1016/j.neuroimage.2011.03.070>

- Mungall, C.J., Torniai, C., Gkoutos, G.V., Lewis, S.E., Haendel, M.A., 2012. Uberon, an integrative multi-species anatomy ontology. *Genome Biol.* 13, R5. <https://doi.org/10.1186/gb-2012-13-1-r5>
- Nagae-Poetscher, L.M., Jiang, H., Wakana, S., Golay, X., van Zijl, P.C.M., Mori, S., 2004. High-resolution diffusion tensor imaging of the brain stem at 3 T. *AJNR Am. J. Neuroradiol.* 25, 1325–1330.
- Naidich, T.P., Duvernoy, H.M. (Eds.), 2009. *Duvernoy's atlas of the human brain stem and cerebellum: high-field MRI: surface anatomy, internal structure, vascularization and 3D sectional anatomy.* Springer, Wien ; New York.
- Nieuwenhuys, R., Voogd, J., van Huijzen, C., 2008. *The human central nervous system, 4th ed. ed.* Springer, New York.
- Nolte, J., 2008. *The Human Brain: An Introduction to its Functional Anatomy.* Mosby.
- Okun, M.S., 2012. Deep-brain stimulation for Parkinson's disease. *N. Engl. J. Med.* 367, 1529–1538. <https://doi.org/10.1056/NEJMct1208070>
- Ooms, P., Mantione, M., Figeet, M., Schuurman, P.R., van den Munckhof, P., Denys, D., 2014. Deep brain stimulation for obsessive-compulsive disorders: long-term analysis of quality of life. *J. Neurol. Neurosurg. Psychiatry* 85, 153–158. <https://doi.org/10.1136/jnnp-2012-302550>
- Paxinos, G., Huang, X., 1995. *Atlas of the Human Brainstem.* Academic Press.
- Poupon, C., n.d. Ginkgo Toolbox [WWW Document]. URL <https://framagit.org/coupon/gkg>
- Prats-Galino, A., Soria, G., de Notaris, M., Puig, J., Pedraza, S., 2012. Functional anatomy of subcortical circuits issuing from or integrating at the human brainstem. *Clin. Neurophysiol. Off. J. Int. Fed. Clin. Neurophysiol.* 123, 4–12. <https://doi.org/10.1016/j.clinph.2011.06.035>
- Quester, R., Schroder, R., 1997. The shrinkage of the human brain stem during formalin fixation and embedding in paraffin. *J Neurosci Methods* 75, 81–9.
- Rushmore, R.J., Wilson-Braun, P., Papadimitriou, G., Ng, I., Rathi, Y., Zhang, F., O'Donnell, L.J., Kubicki, M., Bouix, S., Yeterian, E., Lemaire, J.-J., Calabrese, E., Johnson, G.A., Kikinis, R., Makris, N., 2020. 3D Exploration of the Brainstem in 50-Micron Resolution MRI. *Front. Neuroanat.* 14. <https://doi.org/10.3389/fnana.2020.00040>
- Salamon, N., Sicotte, N., Alger, J., Shattuck, D., Perlman, S., Sinha, U., Schultze-Haakh, H., Salamon, G., 2005. Analysis of the brain-stem white-matter tracts with diffusion tensor imaging. *Neuroradiology* 47, 895–902. <https://doi.org/10.1007/s00234-005-1439-8>
- Setsompop, K., Fan, Q., Stockmann, J., Bilgic, B., Huang, S., Cauley, S.F., Nummenmaa, A., Wang, F., Rathi, Y., Witzel, T., Wald, L.L., 2018. High-resolution in vivo diffusion imaging of the human brain with generalized slice dithered enhanced resolution: Simultaneous multislice (gSlider-SMS). *Magn. Reson. Med.* 79, 141–151. <https://doi.org/10.1002/mrm.26653>
- Solsberg, M.D., 1990. *MR Imaging of the Excised Human Brainstem: A Correlative Neuroanatomic Study* 11.
- Soria, G., De Notaris, M., Tudela, R., Blasco, G., Puig, J., Planas, A.M., Pedraza, S., Prats-Galino, A., 2011. Improved assessment of ex vivo brainstem neuroanatomy with high-resolution MRI and DTI at 7 Tesla. *Anat. Rec. Hoboken NJ* 2007 294, 1035–1044. <https://doi.org/10.1002/ar.21383>
- Stieltjes, B., Kaufmann, W.E., van Zijl, P.C., Fredericksen, K., Pearlson, G.D., Solaiyappan, M., Mori, S., 2001. Diffusion tensor imaging and axonal tracking in the human brainstem. *NeuroImage* 14, 723–735. <https://doi.org/10.1006/nimg.2001.0861>

- Thelwall, P.E., Shepherd, T.M., Stanisz, G.J., Blackband, S.J., 2006. Effects of temperature and aldehyde fixation on tissue water diffusion properties, studied in an erythrocyte ghost tissue model. *Magn. Reson. Med.* 56, 282–289. <https://doi.org/10.1002/mrm.20962>
- Virta, A., Barnett, A., Pierpaoli, C., 1999. Visualizing and characterizing white matter fiber structure and architecture in the human pyramidal tract using diffusion tensor MRI. *Magn. Reson. Imaging* 17, 1121–1133.
- Watson, C., Bartholomaeus, C., Puelles, L., 2019. Time for Radical Changes in Brain Stem Nomenclature—Applying the Lessons From Developmental Gene Patterns. *Front. Neuroanat.* 13. <https://doi.org/10.3389/fnana.2019.00010>
- Wells, W.M., Viola, P., Atsumi, H., Nakajima, S., Kikinis, R., 1996. Multi-modal volume registration by maximization of mutual information. *Med. Image Anal.* 1, 35–51. [https://doi.org/10.1016/s1361-8415\(01\)80004-9](https://doi.org/10.1016/s1361-8415(01)80004-9)
- Wiest-Daesslé, N., Prima, S., Coupé, P., Morrissey, S.P., Barillot, C., 2008. Rician noise removal by non-Local Means filtering for low signal-to-noise ratio MRI: applications to DT-MRI. *Med. Image Comput. Comput.-Assist. Interv. MICCAI Int. Conf. Med. Image Comput. Comput.-Assist. Interv.* 11, 171–179. https://doi.org/10.1007/978-3-540-85990-1_21
- Zou, L., Song, Y., Zhou, X., Chu, J., Tang, X., 2019. Regional morphometric abnormalities and clinical relevance in Wilson’s disease: regional morphometric abnormalities in WD. *Mov. Disord.* 34, 545–554. <https://doi.org/10.1002/mds.27641>